Hindawi
Journal of Nanomaterials
Volume 2023, Article ID 6752950, 7 pages
https://doi.org/10.1155/2023/6752950

Research Article

A Study of Lithium Ferrite and Vanadium-Doped Lithium Ferrite Nanoparticles Based on the Structural, Optical, and Magnetic Properties

S. Malathi,[1] **B. Sridhar**,[2] **and Shiferaw Garoma Wayessa**[3]

[1]*Department of Physics, Muthurangam Government Arts College (Autonomous), Vellore, India*
[2]*Department of Electronics and Communication Engineering, MLR Institute of Technology, Hyderabad, India*
[3]*College of Engineering and Technology, Wollega University, Nekemte, Ethiopia*

Correspondence should be addressed to Shiferaw Garoma Wayessa; shiferawg@wollegauniversity.edu.et

Received 20 September 2022; Revised 20 October 2022; Accepted 24 November 2022; Published 14 February 2023

Academic Editor: B. Deepanraj

Lithium ferrite and vanadium-doped lithium ferrite have been extensively studied in recent research because of their potential applications in thermochromic materials, optoelectronic devices, and as a cathode material for rechargeable lithium batteries. In the present investigation, lithium ferrite and lithium vanadium ferrite are synthesized by sol–gel process. According to the Scherrer formula, the average particle size of lithium ferrite is 22 nm and that of vanadium-doped lithium ferrite is 29 nm. The lattice parameters and dislocation density are calculated from the X-ray diffraction results. According to the Fourier transform infrared spectroscopy analysis, ferrites were formed that exhibit strong absorption bands. According to the energy-dispersive X-ray analysis spectrum, the predicted elements are present in the sample. With the use of a vibrating sample magnetometer (VSM), the materials' magnetic behavior is investigated.

1. Introduction

Recently, considerable attention on synthesis of metal oxide nanoparticles, because of their unique material properties and potential applications, is extending in many fields such as catalysts, electronics devices, solid oxide fuel cells, magnetic storage, and optical materials [1]. Nanotechnology indicates the design, production, and applicability of source materials at various scales of atomic and molecular to establish various nanosized materials. The classification of nanomaterials is based on one, two, and three dimensions [2, 3]. Thin film or manufactured surfaces are under the one-dimension system, and it has been used in electronics industries and engineering. Manufacturing of thin films (sizes 1–100 nm) is now commonplace in the field of solar cells.

Carbon nanotubes (CNTs), which have a diameter of 1 nm and a length of 100 nm, are two-dimensional nanoparticles composed of a layer of graphite coiled up into a cylinder. Three-dimensional nanoparticles are called fullerenes. This is a hollow ball that resembles a soccer ball made of connected carbon pentagons and hexagons. The class of materials known as fullerenes has distinctive physical characteristics. Extreme pressure can be applied to them, and when the pressure is relieved, they can return to their original shape. Fullerenes are empty structures that can be filled with various substances and have potential uses in medicine since they have dimensions that are close to those of several biologically active compounds [4].

The dendrimer is a brand-new class of controlled-structure polymers with nanometric dimensions. Given that they typically range in size from 10 to 100 nm and have a variety of functional groups on their surface, dendrimers are effective drug-delivery vehicles [5]. The small objects called quantum dots have a very small amount of free electrons in them. QDs are colloidal semiconductor nanocrystals with diameters between 2 and 10 nm. Colloidal synthesis or electrochemistry can be used to create QDs from a variety of semiconductor materials. Cadmium selenide (CdSe), cadmium telluride (CdTe), indium phosphide (InP), and indium arsenide are the most widely used QDs (InAs). Nanomedicines, materials, electronics, scientific tools,

environment and energy, and chemical and cosmetics are just a few of the fields where nanotechnology is being used [6]. Numerous technical applications have made extensive use of ferrite material, including the magnetically controlled delivery of anticancer medications, color imaging, gas-sensitive materials, and catalytic materials [7–13]. An extensive survey on various synthesis and characterization techniques of ferrite nanoparticles has been carried out in this paper.

The structural, magnetic, and electrical characteristics of the $Li_{0.5}Fe_{2.5}O_4$ small particles are produced in sol–gel [14]. The sol–gel method was used to view and measure grains that were around 12 nm in size. When the magnetic characteristics of lithium ferrite nanoparticles with grain sizes ranging from 12 to 32 nm were explored, magnetic measurements revealed that the magnetic behavior of the $Li_{0.5}Fe_{2.5}O_4$ small particles deviates from what is expected. The sample displayed a maximum saturation magnetization of 75 emu/g; the change in coercivity is related to the change in nature from multidomain to single-domain.

The structure and its magnetic properties of nanocrystalline $LiFeO_2$ is synthesized by sol–gel method. To confirm the several phases involved in $LiFeO_2$ production, Rietveld analysis was done. According to quantitative Rietveld refinement, the sample comprises 39.9 wt% of cubic $LiFeO_2$, 58.5 wt% of monoclinic $LiFeO_2$, and 1.7 wt% of tetragonal $LiFeO_2$. The particle size distribution is uneven, with an average particle size of 100 nm, as shown by the morphology [15]. At normal temperatures, $LiFeO_2$ powder exhibited spontaneous magnetism. It exhibits ferromagnetic behavior and has a coercivity of 189 Oe and a maximum magnetization value of 0.2 emu/g. SEM examinations revealed nanocrystallinity with 100 nm sized particle size.

Al_2O_3 is used in the evaluation of the nanoparticle production process. Thin films and aluminum oxide nanoparticles are produced using the sol–gel technique. Hitachi S-3400N SEM is used to investigate surface morphologies. Following centrifugation, a particle size between 60 and 90 nm is observed [16]. It has been discovered that the grain size is significantly influenced by the precursors used, the synthesis circumstances, and the aging temperature. The energy bandgap was measured at 4.13 eV. The refractive index was measured between 1.55 and 1.79. The observed value of the extinction coefficient was 0.103. The real and imaginary parts of the dielectric constant were determined to be 2.83 and 0.5, respectively.

By using the sol–gel spin coating process, the pure and aluminum-doped ZnO ($Zn_{1-x}Al_xO$) $x = 0$ to 5 wt% thin films. The aluminum concentrations in ZnO thin films is affected its structural, surface, optical, and photo-conducting characteristics. It is found that doping with aluminum reduces the average grain size. According to AFM images [17], 1.5% of doped films displayed better smoothness than other materials. According to the photoconductivity measurements, the photocurrent for the Al-doped ZnO is greater than the dark current. After attaining its maximum value for ZnO : Al-1.5%, the photocurrent decreases when the concentration of Al is raised.

A new approach to create V_2O_5 nanostructures using the polyvinyl alcohol-based sol–gel process was proposed [18]. In order to create a homogeneous polymeric gel, the precursors NH_4VO_3 and polyvinyl alcohol are dissolved in a binary (ethanol/water) solvent to create a sol solution. SEM, TEM, XRD, and TGA-DTA are used to evaluate the prepared samples. This technique makes it possible to create consistent V_2O_5 nanoflakes with an average thickness of 37 nm. By using cyclic voltammetry, the electrochemical behaviors of V_2O_5 samples are also studied in a 0.1 M $LiClO_4$ electrolyte solution made in a 1 : 1 (V/V) solvent mixture of ethylene carbonate and dimethyl carbonate.

Reactive grinding was used to create nanoparticles of vanadium-doped rutile TiO_2 [19]. As a result of the vanadium doping, size of the particle of vanadium-modified rutile TiO_2 obtained around 22 nm, but under the same conditions, better solar light absorption was found in the 5% vanadium-doped rutile, with an estimated bandgap energy value of 2.7 eV. Lithium nanoferrites with the general formula $Li_{0.5}Al_xFe_{2.5-x}O_4$ were proposed to be synthesized by Aravind and Ravinder [20] using the citrate gel technique at low temperature (1,800°C). The powders produced were sintered for 4 hr at 500°C. The sintered powders' crystal structure was examined using X-ray diffraction (XRD). The average particle size of the synthesized powders ranged from 13 to 27 nm. However, due to vanadium's several oxidation states, materials doped with it showed complex properties [21–24]. Vanadium ions in V-doped $CoFe_2O_4$ nanoferrite are found at the octahedral site for samples doped with less than or equal to 10% V, but some vanadium ions shifted to the tetrahedral position in samples doped with >10% V [25].

According to published research, the type of surfactant and reductant, pH level of the suspension, stirring rate, concentration of precursors, reaction rate, and temperature all affect the structural, electrical, and optical properties of synthesized materials. In this paper, surfactant-free growth and large area uniform of prepared products are discussed.

2. Experimental Method

This work deals with the synthesis of lithium ferrite and vanadium-doped lithium ferrite. Brief descriptions of the various tools in characterizing these samples are also presented.

2.1. Synthesis of Lithium Ferrite through Sol–Gel Route. A well-known colloidal chemistry method called sol–gel gives the ability to create a variety of materials with brand-new, predetermined features through a straightforward process at a reasonably low cost. The chemicals used to synthesize $LiFe_2O_3$ were $Fe(NO_3)_3{\cdot}9H_2O$, $Li(NO_3)$, and citric acid. The acitic acid solution is prepared by sprinkling acitic acid powder in deionized water under continuous stirring to avoid clumping of the material in water. Lithium nitrate and ferric nitrate were dissolved in deionized water in a 1 : 2 ratio to create the sols. After 3 hr of nonstop stirring, citric acid solution was applied to the sols. The resultant mixture was then heated while being constantly stirred to produce the gel. The water molecules were then removed from the gel by keeping it in the muffle furnace for 2 days. The color of the precursor was altered before it was calcinized.

2.2. Synthesis of Lithium Vanadium Ferrite through Sol–Gel Route. The chemicals used to synthesize $LiV_2Fe_2O_3$ were $Fe(NO_3)_3{\cdot}9H_2O$, $Li(NO_3)$, V_2O_5, and citric acid. All of the compounds were of the analytical grade and were utilized directly. In order to prevent the material from clumping in the water, PVA solution was made by slowly sprinkling PVA powder in deionized water while stirring continuously. Lithium nitrate and ferric nitrate were dissolved in deionized water in a 1 : 2 ratio to create the sols. Then, the solution was added to V_2O_5. Three hours of nonstop stirring was followed by the addition of citric acid solution to the sols. The resultant mixture was then heated while being constantly stirred to produce the gel. The water molecules were then removed from the gel by keeping it in the muffle furnace for 2 days. The color of the forerunner was altered. After that, it was ground into a fine powder using a mortar and pestle for an hour. The same technique was used to prepare the sample for vanadium-doped lithium ferrite.

3. Characterization Techniques

Numerous characterization techniques are required to estimate the various properties of the prepared sample. The findings reveal details of the various structural and optical characteristics of the sample. The basis for the occurrence of the diffraction pattern is the unit cell and lattice; it is dispersed in a normal 3D pattern in space. These lattice structures create a collection of several parallel planes, each with distance spacing and varying orientations. Bragg's law is derived from incident monochromatic X-ray reflection from successive crystal lattice planes when the wavelength gap between the planes is n.

$$n\lambda = 2d \sin\theta, \tag{1}$$

where d is the interatomic distance in angstroms, n is an integer (1, 2, 3, etc.), λ is the wavelength in angstroms (1.54 for copper), and θ is the diffraction angle in degrees. The sample-specific pattern is produced by plotting the angular positions and radiation peak intensities that result from the radiation being diffracted. The two areas where XRD has been utilized most frequently are the fingerprint characterization of crystalline materials and the assessment of their structure.

The scanning electron microscope (SEM) uses high-energy electrons to create a variety of signals at the surface of solid specimens. In addition to the sample's exterior morphology (texture), chemical composition, and orientation and crystalline structure of the components that make up the sample, these signals generated by the electrons also provide information about the sample. The sample's surface is often selected for data collection, and a two-dimensional image is made to illustrate the spatial differences in these features. Regions with widths ranging from ~1 cm to 5 μm can be scanned in a scanning mode using conventional SEM techniques.

The UV–vis NIR spectroscopy was used to examine the optical characteristics of the produced nanorods. The apparatus is built to allow for a comparison of the two beams' intensities as it moves over the necessary wavelength range. The substance absorbs light of a specific wavelength, and the sample beams (IS) intensity will be lower than the reference beams. By calculating the radiation's absorption by a sample at various wavelengths and registering the results, the wavelength vs. the absorption (A) of light at each wavelength is shown.

4. Results and Discussion

The synthesized nanoparticles of lithium ferrite and vanadium-doped lithium ferrite are subjected to following characterizations and the properties also incorporated. The impact of V_2 doping on the prepared samples' microstructure was investigated. Due to the formation of cation vacancies and the substitution of Fe with V, the lattice parameter (a) often decreased nonlinearly with the vanadium concentration (x).

4.1. X-Ray Diffraction Analysis. X-ray diffraction analysis to determine the nature of the crystal, its structure, size, strain, and dislocation density is evaluated for the lithium ferrite and vanadium-doped lithium ferrite are done with the help of "D8 Advanced, BRUKER X-Ray Diffractometer" of wavelength $\lambda = 1.5406$ Å. The average particle size of the crystal is evaluated from XRD by using the Debye–Scherrer formula [26, 27] that is given in Equation (2).

$$D = \frac{K\lambda}{\beta \cos\theta}, \tag{2}$$

where D indicates the average size of the crystalline, K represents the Scherrer constant (0.89), λ is the beam wavelength used, β is the full-width half maximum (FWHM) of diffraction, and θ is the Bragg's angle. With the help of the XRD data, we can calculate the strain and dislocation values. Williamson–Hall plot helps to calculate the strain value. The calculated values are tabulated in the Table 1.

The SEM micrographs evident that the $LiFe_2O_4$ and V_2-doped $LiFe_2O_4$ were in the form of nanoparticles which were speculated that the agglomeration of particles. Figures 1 and 2 represent the SEM images of $LiFe_2O_4$ and V_2-doped $LiFe_2O_4$.

4.2. UV–Visible Spectral Study. The UV–vis spectrometer of "JASCO, V-670" was used to evaluate the absorption level of the optical parameters in the nanoparticles. The regions from 200 to 2,500 nm were studied at room temperature. Figure 3 shows the wavelength absorbance graph of $LiFe_2O_4$ and $LiV_2Fe_2O_4$.

The values noted with respect to the cutoff wavelengths for lithium ferrite and vanadium-doped lithium ferrite are 413 and 415 nm, respectively. This demonstrates the viewable region's cutoff. These samples can be utilized to manufacture the semiconductors, optical devices, solar energy conversion devices, etc. The indirect bandgap values for lithium ferrite and vanadium-doped lithium ferrite are 1.01 and 1.01 eV, respectively.

Table 1: Structural properties.

Sr. No.	Properties	$LiFe_2O_4$	$LiV_2Fe_2O_4$
1.	Crystal structure	Monoclinic	Monoclinic
2.	Lattice parameters	$a = 7.748054$ Å $b = 4.797752$ Å $c = 7.516238$ Å $\alpha = \gamma \neq \beta$	$a = 10.22835$ Å $b = 4.92298$ Å $c = 8.717566$ Å $\alpha = \gamma \neq \beta$
3.	Size of the crystal	22 nm	29 nm
4.	Strain	0.6822	0.25934
5.	Dislocation density	$2.066 \times 10^{-15}\ m^{-2}$	$1.1891 \times 10^{-15}\ m^{-2}$

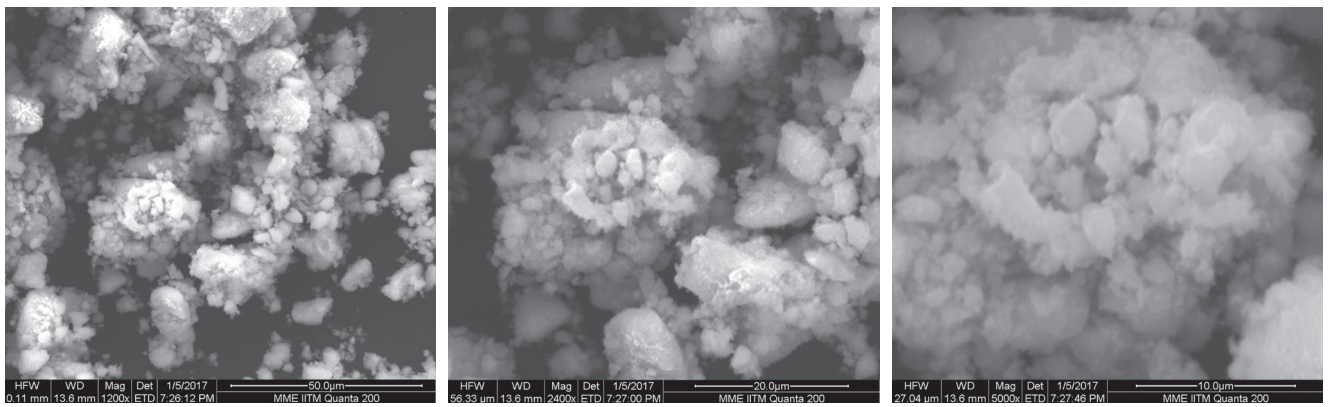

Figure 1: SEM images of $LiFe_2O_4$ nanopowder.

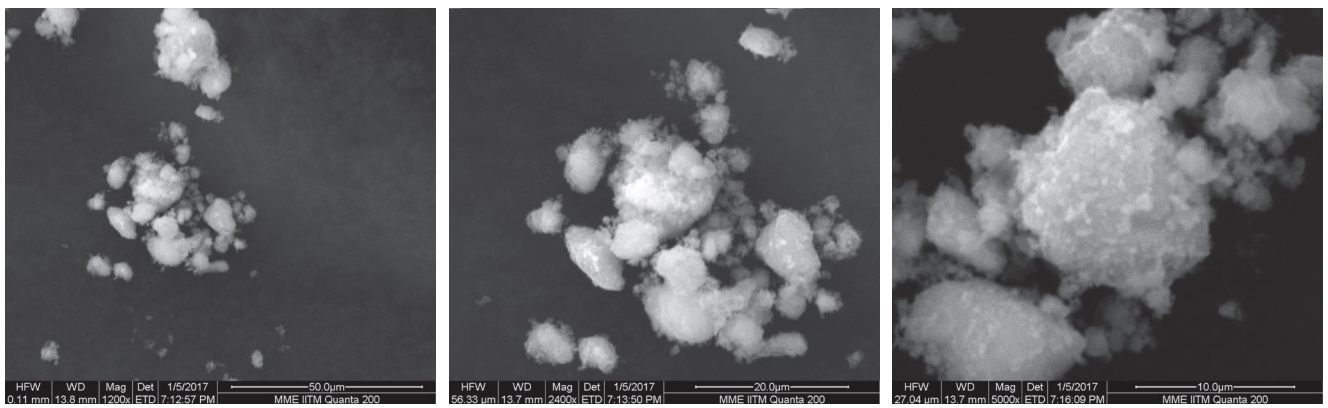

Figure 2: SEM images of V_2-doped $LiFe_2O_4$ nanopowder.

4.3. FTIR Analysis. Fourier transform infrared spectroscopy (FTIR) spectrum analysis is performed for lithium ferrite and vanadium-doped lithium ferrite nanoparticles in the range of 400–4,000 cm^{-1}. The FTIR analysis shows that the change in temperature changes the nature of the bond of the samples. The peak range of both the samples ranges from 3,200 to 3,600 shows the O—H bond. Figures 4 and 5 describe the FTIR spectrum for $LiFe_2O_4$ and $LiV_2Fe_2O_4$.

The range of 1,620–1,680 corresponds to the bond present as C═C. The value range of 1,350–1,480 shows —C—H bond. 866.04 cm^{-1} for lithium ferrite corresponds ═C—H bond. The values of vanadium-doped lithium ferrite for the ranges 675–1,000 correspond to ═C—H bond.

4.4. Vibrating Sample Microscope. The vibrating sample micrograph at room temperature for both the samples is

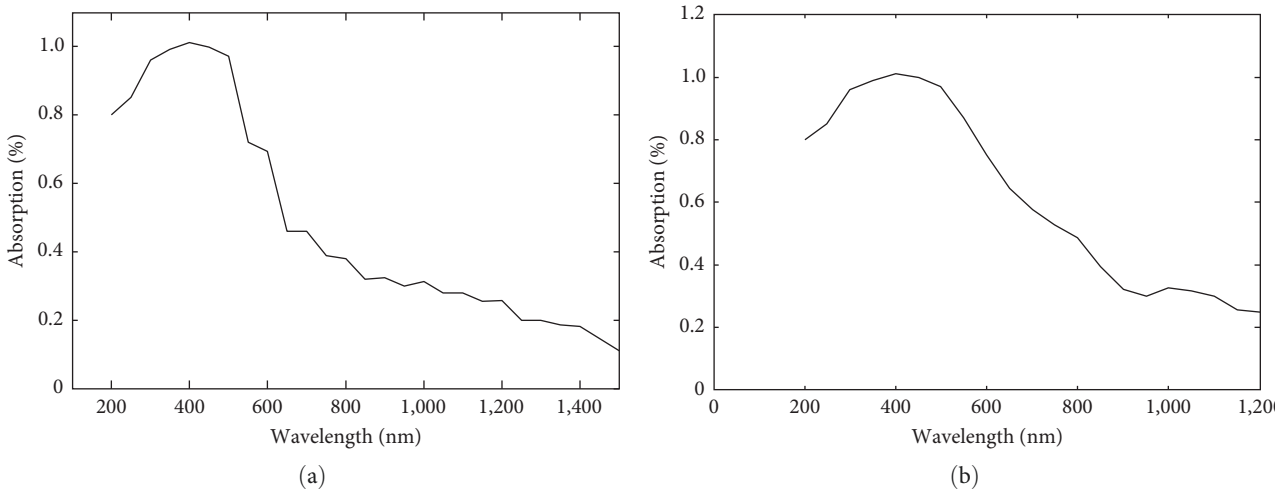

FIGURE 3: (a) Wavelength–absorbance graph of $LiFe_2O_4$; (b) wavelength–absorbance graph of $LiV_2Fe_2O_4$.

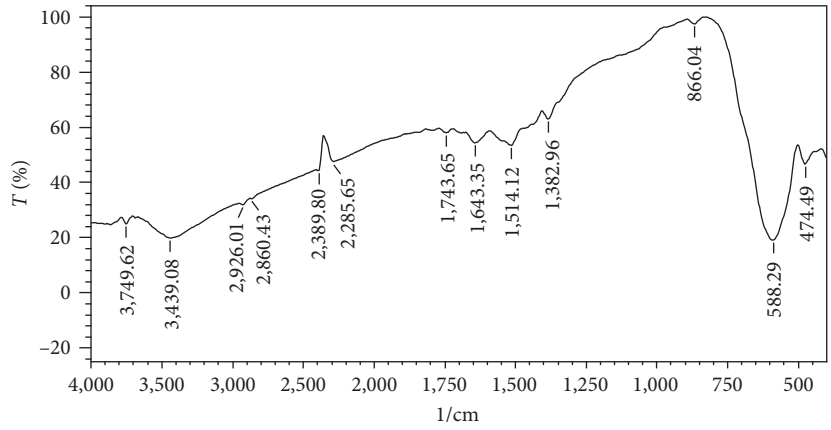

FIGURE 4: FTIR spectrum of $LiFe_2O_4$.

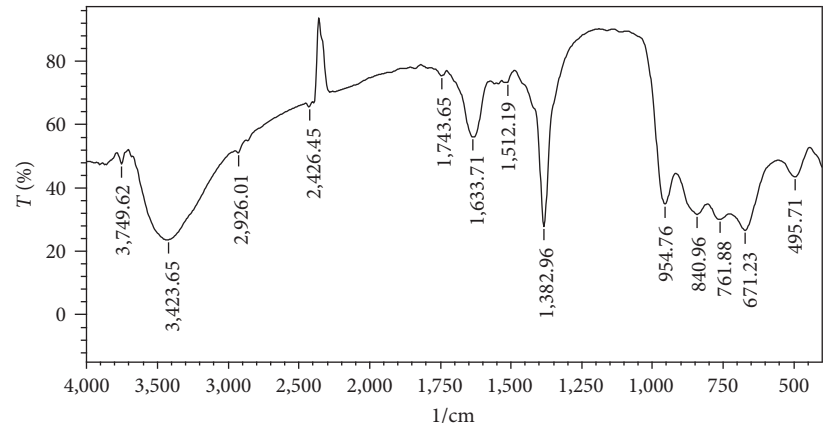

FIGURE 5: FTIR spectrum of $LiV_2Fe_2O_4$.

shown. The corresponding magnetic properties are listed in Table 2.

Both samples' natures demonstrate excellent soft magnetic properties and extraordinary paramagnetic behavior [28–30]. Figures 6 and 7 represent the VSM graph for $LiFe_2O_4$ and $LiV_2Fe_2O_4$. Due to their low coercive values, these ferrites can be employed to create magnetic storage devices and other objects without causing any flux loss or

Table 2: Magnetic properties.

Sr. No.	Properties	$LiFe_2O_4$	$LiV_2Fe_2O_4$
1.	Coercivity	16.099 G	2.4305 G
2.	Magnetization	0.58657 emu	18.795^{-3} emu
3.	Retentivity	5.3467 emu	4.8057^{-6} emu

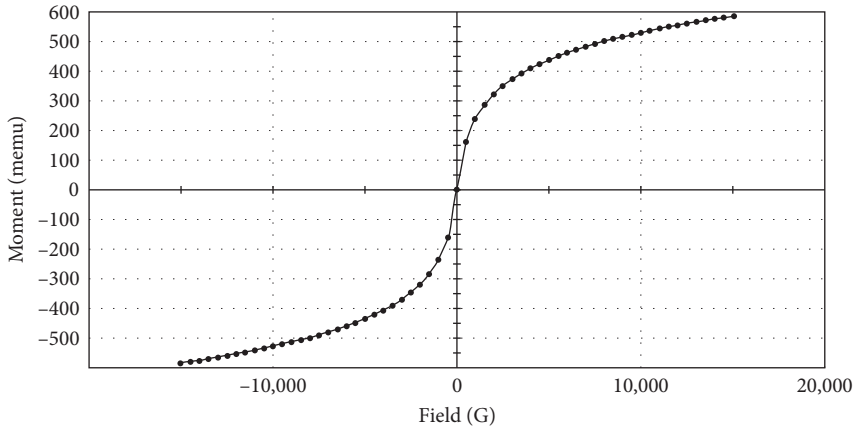

Figure 6: VSM graph of $LiFe_2O_4$.

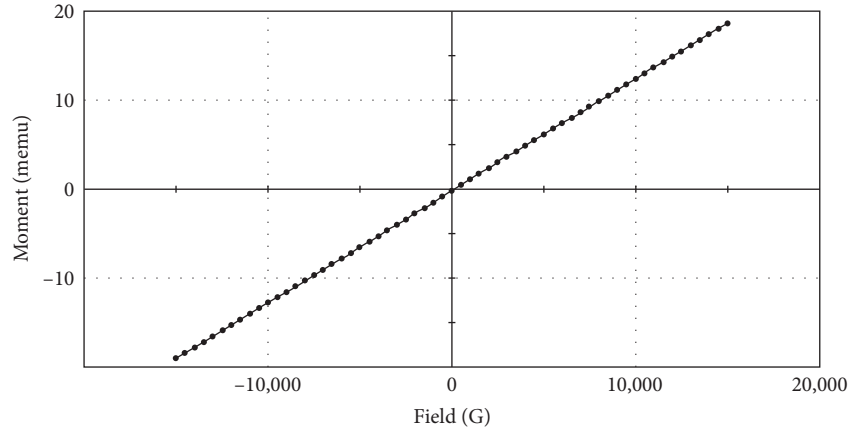

Figure 7: VSM graph of $LiV_2Fe_2O_4$.

difficulty magnetizing the particles. Ferrites, notably magnetoplumbite and spinel ferrite, can be used as pigments, microwave devices, recording media, and other things.

Due to its high-saturation magnetization and high coercivity, strontium ferrite has drawn more scientific study recently compared to magnetoplumbite ferrites and spinel ferrite.

5. Conclusion

The nanoparticles of lithium ferrite and vanadium-doped lithium ferrite are prepared with the help of sol–gel synthesis. The XRD data show the samples are monoclinic in structure. The strain values and dislocation density are also calculated. The particle size is in the range of 22–29 nm. The UV–vis values show the cutoff value present in the visible region. So, we can use these materials in making optoelectronic devices like photovoltaic cells, photoconduction cells, photodiodes, lasers, CD players, etc. The VSM results reveal that the samples have a superparamagnetic nature, so it is possible that these materials may be used to make pigments, humidity sensors, microwave devices, recording media, and other things. Due to their high-saturation magnetization, high coercivity, and high uniaxial magnetic anisotropy, strontium ferrites have recently drawn more scientific attention than magnetoplumbite ferrite and spinel ferrite.

Data Availability

The datasets generated and/or analyzed during the current study are available from the corresponding author on reasonable request.

Conflicts of Interest

The authors declare that they have no conflicts of interest.

References

[1] W. I. Hagens, A. G. Oomen, W. H. de Jong, F. R. Cassee, and A. J. A. M. Sips, "What do we (need to) know about the kinetic properties of nanoparticles in the body?" *Regulatory Toxicology and Pharmacology*, vol. 49, no. 3, pp. 217–229, 2007.

[2] A. Hett, *Nanotechnology: Small Matters, Many Unknown*, Swiss Reinsurance Company, 2004.

[3] M. Köhler and W. Fritzsche, *Nanotechnology: An Introduction to Nanostructuring Techniques*, Wiley, Weinheim, 2004.

[4] D. A. Tomalia, "Dendrimer as quantized building blocks for nanoscale synthetic organic chemistry," *Aldrichmica Acta*, vol. 37, no. 2, pp. 39–57, 2004.

[5] E. Wiener, M. W. Brechbiel, H. Brothers et al., "Dendrimer-based metal chelates: a new class of magnetic resonance imaging contrast agents," *Magnetic Resonance in Medicine*, vol. 31, no. 1, pp. 1–8, 1994.

[6] Y. Li, Y. Cheng, and T. Xu, "Design, synthesis and potent pharmaceutical applications of glycodendrimers: a mini review," *Current Drug Discovery Technologies*, vol. 4, no. 4, pp. 246–254, 2007.

[7] N. M. Deraz and S. Shaban, "Optimization of catalytic, surface and magnetic properties of nanocrystalline manganese ferrite," *Journal of Analytical and Applied Pyrolysis*, vol. 86, no. 1, pp. 173–179, 2009.

[8] N. M. Deraz, M. K. El-Aiash, and S. A. Ali, "Novel preparation and physicochemical characterization of a nanocrystalline cobalt ferrite system," *Adsorption Science & Technology*, vol. 27, no. 8, pp. 797–810, 2009.

[9] N. M. Deraz, A. Alarifi, and S. A. Shaban, "Removal of sulfur from commercial kerosene using nanocrystalline $NiFe_2O_4$ based sorbents," *Journal of Saudi Chemical Society*, vol. 14, no. 4, pp. 357–362, 2010.

[10] Y. Köseoğlu, A. Baykal, F. Gözüak, and H. Kavas, "Structural and magnetic properties of $Co_xZn_{1-x}Fe_2O_4$ nanocrystals synthesized by microwave method," *Polyhedron*, vol. 28, no. 14, pp. 2887–2892, 2009.

[11] S.-W. Cao, Y.-J. Zhu, G.-F. Cheng, and Y.-H. Huang, "$ZnFe_2O_4$ nanoparticles: microwave-hydrothermal ionic liquid synthesis and photocatalytic property over phenol," *Journal of Hazardous Materials*, vol. 171, no. 1–3, pp. 431–435, 2009.

[12] Z. H. Zhou, J. M. Xue, J. Wang, H. S. O. Chan, T. Yu, and Z. X. Shen, "$NiFe_2O_4$ nanoparticles formed *in situ* in silica matrix by mechanical activation," *Journal of Applied Physics*, vol. 91, no. 9, Article ID 6015, 2002.

[13] Y. Köseoğlu, F. Yıldız, G. Slazar-Alvarez, M. Toprak, M. Muhammed, and B. Aktaş, "Synthesis, characterization and ESR measurements of CoNiO nanoparticles," *Physica Status Solidi (b)*, vol. 42, no. 8, pp. 1712–1718, 2005.

[14] M. George, S. S. Nair, A. M. John, P. A. Joy, and M. R. Anantharaman, "Structural, magnetic and electrical properties of the sol–gel prepared $Li_{0.5}Fe_{2.5}O_4$ fine particles," *Journal of Physics D: Applied Physics*, vol. 39, no. 5, Article ID 900, 2006.

[15] K. Vijaya Kumar, A. Sangeetha, A. T. Raghavender, Z. Skoko, and G. Nanda Kumar, "Rietveld refinement of nanocrystalline $LiFeO_2$ synthesized by sol–gel method and its structural and magnetic properties," *Journal of Crystallization Process and Technology*, vol. 2, no. 4, pp. 152–155, 2012.

[16] F. Majid, S. Riaz, M. I. Akram, S. Atiq, and S. Naseem, "Preparation and characterization of electrodeposited aluminum oxide thin films," in *International Conference on Advanced Computer Science and Electronics Information (ICACSEI 2013)*, pp. 523–526, Atlantis Press, August 2013.

[17] T. Ganesh, S. Rajesh, and F. P. Xavier, "Sol–gel preparation, deposition and characterization of nanostructured aluminium doped zinc oxide," *Journal of Nano Research*, vol. 24, pp. 96–106, 2013.

[18] H. Karami and A. Mohammadi, "Poly vinyl alcohol-based sol–gel synthesis of V_2O_5 nanoflakes as positive electrodes of Li-ion batteries," *International Journal of Electrochemical Science*, vol. 10, pp. 7392–7408, 2015.

[19] T. M. Nguyet Tran, T. H. Yen Quach, Q. C. Tran et al., "Synthesis of vanadium-modified rutile TiO_2 nanoparticle by reactive grinding method and its photocatalytic activity under solar light at room temperature," *Advances in Natural Sciences: Nanoscience and Nanotechnology*, vol. 4, no. 3, Article ID 035010, 2013.

[20] G. Aravind and D. Ravinder, "Preparation and structural properties of aluminium substituted lithium nano ferrites by citrate-gel auto combustion method," *International Journal of Engineering Research and Applications*, vol. 3, no. 6, pp. 1414–1421, 2013.

[21] Z. K. Heiba, M. B. Mohamed, A. M. Wahba, and M. I. Almalowi, "Effect of vanadium doping on structural and magnetic properties of defective nano-nickel ferrite," *Applied Physics A*, vol. 124, Article ID 290, 2018.

[22] M. A. Almessiere, Y. Slimani, H. Güngüneş, H. S. El Sayed, and A. Baykal, "AC susceptibility and hyperfine interactions of vanadium substituted barium nanohexaferrites," *Ceramics International*, vol. 44, no. 15, pp. 17749–17758, 2018.

[23] A. D. Korkmaz, S. Güner, Y. Slimani et al., "Microstructural, optical, and magnetic properties of vanadium-substituted nickel spinel nanoferrites," *Journal of Superconductivity and Novel Magnetism*, vol. 32, pp. 1057–1065, 2019.

[24] M. A. Almessiere, Y. Slimani, and A. Baykal, "Structural, morphological and magnetic properties of hard/soft $SrFe_{12-x}V_xO_{19}/(Ni_{0.5}Mn_{0.5}Fe_2O_4)y$ nanocomposites: effect of vanadium substitution," *Journal of Alloys and Compounds*, vol. 767, pp. 966–975, 2018.

[25] Z. K. Heiba, M. B. Mohamed, and S. I. Ahmed, "Cation distribution correlated with magnetic properties of cobalt ferrite nanoparticles defective by vanadium doping," *Journal of Magnetism and Magnetic Materials*, vol. 441, pp. 409–416, 2017.

[26] V. Chithambaram, T. S. Franklin Rajesh, G. Palani, E. Ilango, B. Deepanraj, and S. Santhanakrishnan, "Growth and investigation of novel nonlinear optical single crystal of urea potassium dichromate by solution growth technique for photonic application," *Journal of Optics*, vol. 49, pp. 181–186, 2020.

[27] B. D. Cullity, *Elements of X-ray Diffraction*, Addison-Wesley Publishing Co. Inc., 1976.

[28] I. Zālīte, G. Heidemane, M. Kodols, J. Grabis, and M. Maiorov, "The synthesis, characterization and sintering of nickel and cobalt ferrite nanopowders," *Materials Science*, vol. 18, no. 1, 2012.

[29] S. Shanmugan, N. Saravanan, V. Chithambaram, B. Deepanraj, and G. Palani, "Investigation on single crystal by tartaric acid–barium chloride: growth and characterization of novel NLO materials," *Bulletin of Materials Science*, vol. 43, Article ID 202, 2020.

[30] S. Rehman, A. Mumtaz, and S. K. Hasanain, "Size effects on the magnetic and optical properties of CuO nanoparticles," *Journal of Nanoparticle Research*, vol. 13, pp. 2497–2507, 2011.